nanomaterials

MDPI

Article

Enhanced Methane Sensing Properties of WO_3 Nanosheets with Dominant Exposed (200) Facet via Loading of SnO_2 Nanoparticles

Dongping Xue [1,2], Junjun Wang [1,3,*], Yan Wang [1,4], Guang Sun [1,2], Jianliang Cao [1,2], Hari Bala [1,2] and Zhanying Zhang [1,2,*]

1 The Collaboration Innovation Center of Coal Safety Production of Henan Province, Henan Polytechnic University, Jiaozuo 454000, China; xdongping1231@126.com (D.X.); yanwang@hpu.edu.cn (Y.W.); mcsunguang@163.com (G.S.); caojianliang@hpu.edu.cn (J.C.); hari@hpu.edu.cn (H.B.)
2 Institute of Materials Science and Engineering, Henan Polytechnic University, Jiaozuo 454000, China
3 Institute of Physics & Electronic Information Engineering, Henan Polytechnic University, Jiaozuo 454000, China
4 Institute of Safety Science and Engineering, Henan Polytechnic University, Jiaozuo 454000, China
* Correspondence: junjun.wang@hpu.edu.cn (J.W.); zhangzy@hpu.edu.cn (Z.Z.)

Received: 6 February 2019; Accepted: 20 February 2019; Published: 4 March 2019

Abstract: Methane detection is extremely difficult, especially at low temperatures, due to its high chemical stability. Here, WO_3 nanosheets loaded with SnO_2 nanoparticles with a particle size of about 2 nm were prepared by simple impregnation and subsequent calcination using SnO_2 and $WO_3 \cdot H_2O$ as precursors. The response of SnO_2-loaded WO_3 nanosheet composites to methane is about 1.4 times higher than that of pure WO_3 at the low optimum operating temperature (90 °C). Satisfying repeatability and long-term stability are ensured. The dominant exposed (200) crystal plane of WO_3 nanosheets has a good balance between easy oxygen chemisorption and high reactivity at the dangling bonds of W atoms, beneficial for gas-sensing properties. Moreover, the formation of a n–n type heterojunction at the SnO_2-WO_3 interface and additionally the increase of specific surface area and defect density via SnO_2 loading enhance the response further. Therefore, the SnO_2-WO_3 composite is promising for the development of sensor devices to methane.

Keywords: SnO_2-loaded WO_3 nanosheets; methane sensing; heterojunction; exposed (200) facet

1. Introduction

The gas detection of methane is significantly important in coalmine production, usage of natural gas, atmospheric monitoring, etc. However, due to the high chemical stability of the C–H bond in methane, methane detection is extremely difficult, especially at low temperatures. Therefore, it is important to develop a reliable, sensitive sensor that can detect methane at low temperatures. Metal oxide semiconductor (MOS) sensors have attracted extensive attention due to their low cost, high sensitivity, fast response/recovery, and easy integration [1–4]. However, the applications of these MOS sensors are limited due to their high operating temperature and poor stability [5–7]. In order to reduce the operating temperature and improve the stability and sensitivity of different MOS gas sensors, methods such as noble metal/transition metal doping, heterojunction formation and unique surface morphology have been studied [8–13].

WO_3 is one of the most promising gas-sensitive materials due to its moderate energy band, rich oxygen vacancies and high response. In particular, since Akiyama et al. started their work, the gas-sensing characteristics of WO_3 have been well studied due to the high sensitivity of WO_3 to various gases [14]. It is well known that the gas-sensing properties of MOS materials are

considerably dependent on their morphology [15,16]. Hence, many unique WO_3 nanostructures, such as nanosheets [17–19], nanorods [20], nanowires [21,22] and nanospheres [23,24], have been synthesized to improve the gas sensitivity of gas sensors. Among these topographies, 2D nanosheets having a flat surface and a regular shape have attracted great attention in various fields due to their good optical and electrical properties [25]. SnO_2 has become one of the most widely studied nanomaterials due to its unique properties [2,26]. The SnO_2-WO_3 hybrid structure has received great attention because SnO_2 and WO_3 have different degrees of reaction to various redox gases, moderate resistivity, significant catalytic activity, high stability, low cost and unique gas-sensing characteristics [27–34]. When an n–n type heterojunction is formed at the interface between SnO_2 and WO_3, the Fermi levels of the two constitute materials across the heterojunction equilibrate to the same energy level leading to charge transfer and consequently the formation of a space charge region serving as the basis of the increase of sensor response [35]. However, very few studies have been reported regarding methane sensing employing the SnO_2-WO_3 hybrid structure.

In this work, we investigated the methane gas-sensing properties of SnO_2-WO_3 hybrid structures. We successfully prepared WO_3 nanosheets using a simple one-step hydrothermal method, and added a small number of SnO_2 nanoparticles with a particle size of about 2 nm using the impregnation method to obtain SnO_2-WO_3 nanocomposites. Our study showed that the SnO_2-WO_3 nanocomposite had higher sensitivity to methane than pure WO_3 nanosheets and that the optimum operating temperature of both sensors was relatively low at 90 °C. The crystal structure, morphology, specific surface area, and pore-size distribution of the as-prepared pure and SnO_2-loaded WO_3 nanosheets were investigated using various characterization tools. Gas-sensing properties were tested systematically and the gas-sensing mechanism was thoroughly discussed with the focus on the influence of the heterojunction and the observed dominant surface facet of the WO_3 nanosheets.

2. Experimental Details

2.1. Preparation of WO_3 H_2O Nanosheets, SnO_2 Nanoparticles and Their Composite

All chemical reagents used in the experiments, including sodium tungstate ($Na_2WO_4{\cdot}2H_2O$, 99.5%), stannic chloride pentahydrate ($SnCl_4{\cdot}5H_2O$, 99%), nitric acid (HNO_3, 65%), polyethylene glycol 400 (PEG-400), sodium hydroxide (NaOH, 98%), aqueous ammonia ($NH_3{\cdot}H_2O$ 25–28%), and absolute ethanol were of analytical grade and as received without any further purification. Distilled water was used throughout the experiments.

Both the $WO_3{\cdot}H_2O$ nanosheets and the SnO_2 nanoparticles were synthesized through a one-step hydrothermal method. In a typical synthesis of $WO_3{\cdot}H_2O$ nanosheets, 0.323 g sodium tungstate ($Na_2WO_4{\cdot}2H_2O$) was dissolved in 15 mL of distilled water under continuous stirring, and 10 mL of HNO_3 solution was added. After vigorous stirring for 10 min, the obtained mixture was transferred into a 50 mL stainless autoclave lined with a Teflon vessel and maintained at 180 °C for 12 h. After naturally cooling down, the precipitates were collected by centrifugation, washed with distilled water and absolute ethanol for several times and then dried in the air at 60 °C for 12 h.

For synthesis of SnO_2 nanoparticles, 5 mL of $SnCl_4{\cdot}5H_2O$ ethanol solution (1 M) was added to 90 mL of 50% diluted ethanol solution and 5 mL of $NH_3{\cdot}H_2O$ was added to form a homogeneous suspension under magnetic stirring. The suspension was transferred into a 100 mL stainless autoclave lined with a Teflon vessel and maintained at 150 °C for 24 h. After naturally cooling down, the as-synthesized sample was collected, washed, and dried as described for $WO_3{\cdot}H_2O$.

To prepare the SnO_2-WO_3 composites, the above synthesized $WO_3{\cdot}H_2O$ nanosheets 0.04 g, SnO_2 nanoparticles 0.002 g were dissolved in 5 mL of distilled water, underwent ultrasonic treatment for 2 h and then were dried at 60 °C for 6 h. Finally, the obtained precipitates were annealed at 450 °C for 2 h to strengthen the chemical bonding between SnO_2 and WO_3.

2.2. Material Characterization

The crystalline structure and phase of the samples were investigated by X-ray diffraction (XRD, Bruker-AXS D8, Bruker, Madison, WI, USA) with Cu Kα radiation at 40 kV and 150 mA in a scanning range of 20–80° (2θ) in steps of 0.02°. The morphologies and nanostructures were investigated by field-emission scanning electron microscopy (FESEM, Quanta™ FEG 250) (FEI, Eindhoven, The Netherlands) and transmission electron microscopy (TEM) analysis is performed on a Tecnai G2 F20 microscope (FEI, Eindhoven, The Netherlands) operating at 200 kV. UV-vis absorption spectra were obtained on a UV-vis diffuse reflection spectrometer (TU1901) (General Analytical Instruments Company, Beijing, China). N_2 adsorption–desorption was performed on a Quantachrome Autosorb-iQ sorption analyzer (Quantachrome, Boynton Beach, FL, USA). The specific surface area of the products was calculated following the multi-point Brunauer–Emmett–Teller (BET) procedure.

2.3. Gas-Sensing Measurement

The fabrication of the sensor is similar to our previously reported work [36,37]. The samples were mixed with distilled water to form a homogeneous paste and coated onto a ceramic substrate (13.4 mm × 7 mm) with an Ag-Pd interdigitated electrode (Figure 1). Gas-sensing tests were carried out on an intelligent gas-sensing analysis system of CGS-4TPS (Beijing Elite Tech Co., Ltd., Beijing, China) under laboratory conditions (20 RH%, 25 °C). The sensor response was defined as R_a/R_g, where R_a and R_g represent the resistance of the sensor in air and target gas, respectively.

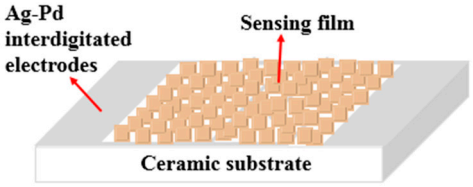

Figure 1. Schematic diagram of a gas sensor.

3. Results and Discussion

3.1. Characterizations of the As-Prepared Samples

To investigate the effect of the loading of SnO_2 nanoparticles on WO_3, XRD analysis of the samples is shown in Figure 2. All the diffraction peaks of pure WO_3 were in complete agreement with monoclinic WO_3 (JCPDS file No. 43−1035), and no diffraction peaks of other impurities was found, indicating that the pure sample was a crystalline phase with high-purity WO_3. No SnO_2 diffraction peak was found in the XRD diffraction pattern of SnO_2-WO_3 sample, presumably due to its low load (5 wt.%). However, the peak position was shifted compared to the pure WO_3 diffraction peak, as shown in the inset of Figure 2; the shift in peak positions $\Delta(2\theta)$ was found to be ~0.09° and 0.05° for SnO_2-WO_3 with respect to pure WO_3, speculatively due to the interaction between SnO_2 and WO_3.

The morphology and structural characteristics of the samples were characterized by FESEM and TEM as shown in Figure 3. Figure 3a,c shows the typical FESEM images of WO_3 nanosheets and SnO_2-WO_3 nanocomposites, and the insets are the respective enlarged FESEM images. It can be clearly seen that both samples were composed of nanosheets with a side length of about 100 nm. The SnO_2 nanoparticles in the composite were too small and too few to be seen with limited magnification. The pure WO_3 nanosheets had a more uniform distribution, more uniform particle size, and more regular and smoother surface than the SnO_2-loaded ones. Figure 3b shows the TEM image of the SnO_2 nanoparticles, the inset of which is the TEM image of the same sample with an even higher magnification. The SnO_2 nanoparticles have a particle size of about 2 nm and are evenly distributed. Figure 3d presents the TEM image of the SnO_2-WO_3 nanocomposite. As can be seen, the SnO_2 nanoparticles are preferably dispersed on the WO_3 nanosheets. Figure 3e shows the high-resolution

transmission electron microscopy (HRTEM) image of the SnO_2-WO_3 nanocomposite, where the lattice spacing of 0.188 nm and 0.384 nm can be indexed to the (040) and (002) crystal planes of the monoclinic WO_3 phase, respectively. Therefore, the dominant exposed facet of the WO_3 nanosheets can be determined to be the (200) facet. The strongest diffraction peak in the XRD patterns is indexed to the (200) crystal plane indicating the preferential growth crystal plane, being consistent with the exposed surface facet. Moreover, the lattice spacing of SnO_2 as 0.264 nm and 0.334 nm are indexed to the (101) and (110) crystal planes of the tetragonal rutile SnO_2 phase, respectively. Figure 3f presents the selected area electron diffraction (SAED) diagram of a single SnO_2-loaded WO_3 nanosheet from Figure 3d. It can be clearly seen that the WO_3 nanosheet is a single crystal, but the diffraction spots are not periodically distributed, probably due to the existence of two phases; firstly, WO_3, and secondly, SnO_2. To further prove that the SnO_2 is indeed loaded onto the WO_3 nanosheets, the SnO_2-WO_3 nanocomposites were characterized by energy-dispersive X-ray spectroscopy (EDS) techniques as shown in Figure 3g–i, and it is obvious that W, O and Sn elements are present in the composite.

UV-vis absorption spectra of pure and SnO_2-loaded WO_3 are shown in Figure 4. A red shift is observed for the absorption spectrum of SnO_2-WO_3 as compared to that of WO_3. The inset of Figure 4 shows the relationship between $(\alpha hv)^2$ and photon energy hv, where α is the absorption coefficient, h the Planck constant, and v the light frequency. Extrapolating the part of the spectra near the absorption edge, the intersection with the abscissas is obtained as the band gap, 2.62 eV and 2.57 eV for pure and SnO_2-loaded WO_3, respectively. This indicates that the band gap of WO_3 is narrowed due to the modification of SnO_2 nanoparticles, beneficial for electron transition and therefore for the oxygen chemisorption at the surface. Meanwhile, the modified band structure of WO_3 is proof of the heterojunction between SnO_2 and WO_3 [38–40]. Simultaneously, the shape change of the absorption spectrum for SnO_2-WO_3 composite at some wavelengths, e.g., 340–360 nm, indicates that the band structure of WO_3 in the composite is modified by loading SnO_2 and consequently, SnO_2-WO_3 composite is definitely not two individual materials without chemical bonding between them.

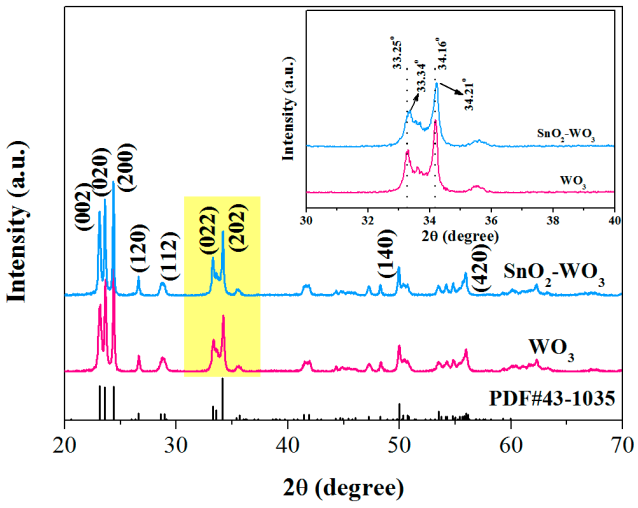

Figure 2. XRD patterns of the as-prepared pure WO_3 and SnO_2-WO_3 nanocomposite.

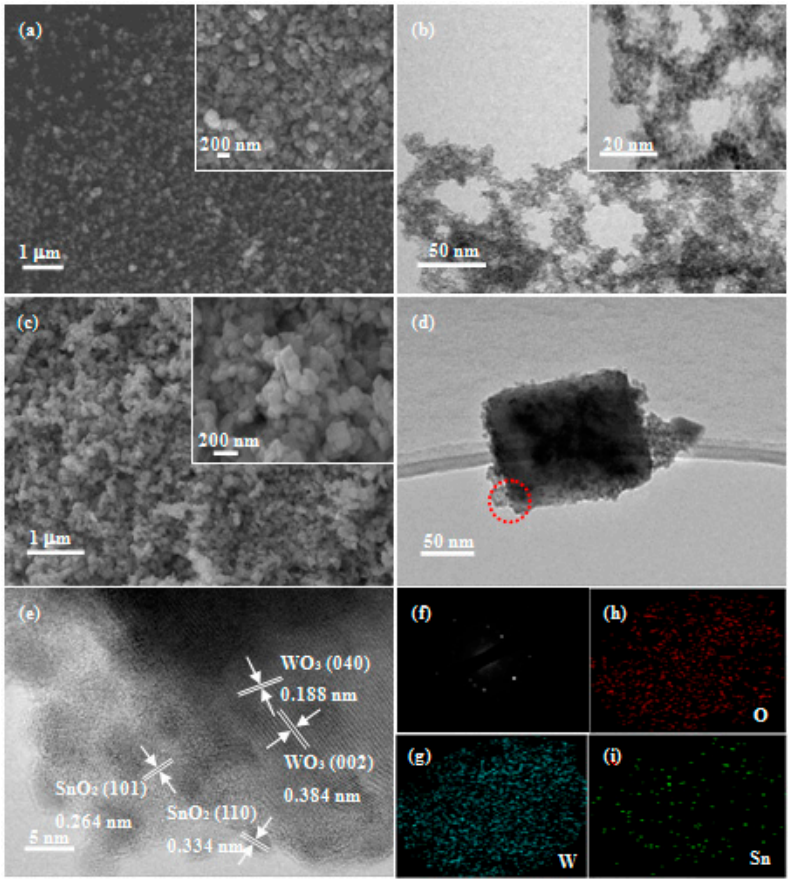

Figure 3. Field-emission scanning electron microscopy (FESEM) images of (**a**) WO_3 nanosheets and (**c**) SnO_2-WO_3 nanosheets. FETEM images of (**b**) SnO_2 nanoparticles and (**d**) SnO_2-WO_3 nanosheets. (**e**) High-resolution transmission electron microscopy (HRTEM) image, (**f**) selected area electron diffraction (SAED) image and (**g**–**i**) energy-dispersive X-ray spectroscopy (EDS) image of SnO_2-WO_3 nanosheets.

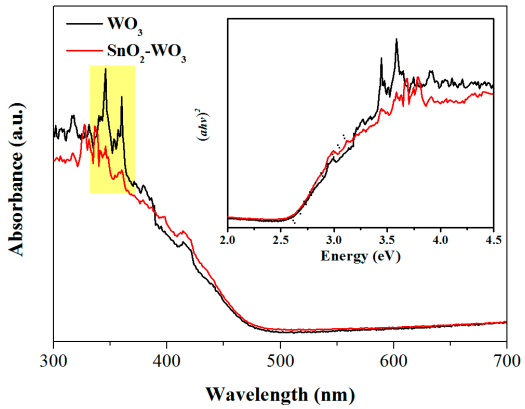

Figure 4. UV–vis absorption spectra of the pure WO_3 and SnO_2-WO_3 nanosheets. The inset shows the relationship between $(\alpha h\nu)^2$ and $h\nu$.

The specific surface area and pore-size distribution of the pure and SnO_2-loaded WO_3 were estimated by N_2 adsorption–desorption. As shown in Figure 5a,b, two samples exhibit a IV-type adsorption isotherm with a H3-type hysteresis loop. The specific surface areas of pure WO_3 and SnO_2-WO_3 were calculated by the BET method to be 10.5 m^2/g and 57.7 m^2/g, respectively. From the inset of Figure 5a, the pore-size distribution range of pure WO_3 is estimated to be mainly 1.3 nm–14.6 nm. According to the SEM image (Figure 3), these pores can be attributed to random

stacking of WO_3 nanosheets. The inset of Figure 5b reveals the main pore size of the SnO_2-WO_3 sample ranges from 2.6 nm to 4.7 nm. It can be inferred from the TEM image that these pores are mainly formed by the distribution of SnO_2 nanoparticles on WO_3 nanosheets, and the loading of the SnO_2 nanoparticles makes the pore-size distribution of the composite more uniform.

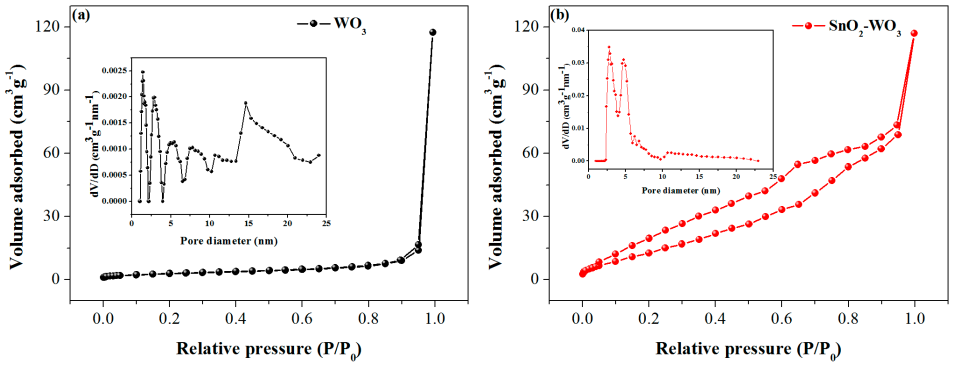

Figure 5. N_2 adsorption and desorption isotherms of (**a**) pure WO_3 nanosheets and (**b**) SnO_2-WO_3 nanosheets with their corresponding pore-size distribution (inset).

3.2. Gas-Sensing Properties

Gas sensors based on pure and SnO_2-loaded WO_3 nanosheets were prepared and their series of gas-sensing properties for methane were investigated. Since working temperature has a great influence on the gas-sensing performance, the dependence of the sensor response on working temperature was investigated with 500 ppm of the methane concentration. The response firstly increased with an increasing operating temperature, up to an optimum operating temperature of 90 °C, then saturated and dropped with a further rising temperature (Figure 6). This may be because the chemisorbed oxygen reached the energy required to react with the methane molecules, so an effective reaction at the surface of the material caused a significant change in electrical resistance [41]. Importantly, the response of the SnO_2-loaded WO_3 sensor was enhanced as compared to that of pure WO_3 in the temperature range of 50–140 °C, by a maximum factor of 1.4 at 90 °C, indicating that the loading of the SnO_2 nanoparticles had an obvious effect of improving the gas sensitivity of the WO_3-based methane sensor. The response dependent on the methane partial pressure at 90 °C was investigated for both sensors (Figure 7a) [42,43]. As expected, the response of both sensors increased with an increasing methane partial pressure. Both the rising slope and the response value of SnO_2-loaded WO_3 were greater than those of pure WO_3. The dynamic response curves of the pure and SnO_2-loaded WO_3 sensor to different methane concentrations were measured (Figure 7b). The response of the SnO_2-WO_3 sensor was always higher than that of the pure WO_3 sensor with increasing methane concentration and recovered to the base value when the sensor was exposed to air after multiple operation cycles. The inset in Figure 7b shows the amplified response/recovery curve for the methane concentration of 5 ppm. According to the inset, full recovery was achieved and the slope of the response decreases with time indicating the response was approaching saturation. The slow response/recovery was caused by the low working temperature and the strong stability of methane molecules. This phenomenon has been observed by other reports on the detection of methane [4,44,45]. Methods of achieving rapid response/recovery at low working temperatures still need to be investigated. From Figure 7b, it is clear that the initial slope of the dynamic response curve of the SnO_2-WO_3 sensor is larger than that of the pure WO_3 sensor, presumably due to the increased number of active sites [46], which will be discussed in Section 3.3. Repeatability and long-term stability are also important parameters for the practical application of a sensor. As shown in Figure 8a,b, the SnO_2-WO_3 sensor could maintain response/recovery performance without major changes after four operation cycles, and the response was kept within 90% of the initial value during 30 days, revealing that the sensor had good repeatability and long-term stability.

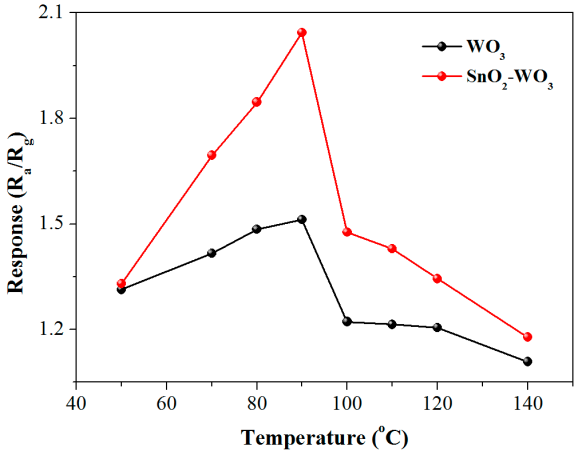

Figure 6. Response of pure WO_3 and SnO_2-WO_3 sensors to 500 ppm methane at different operating temperatures.

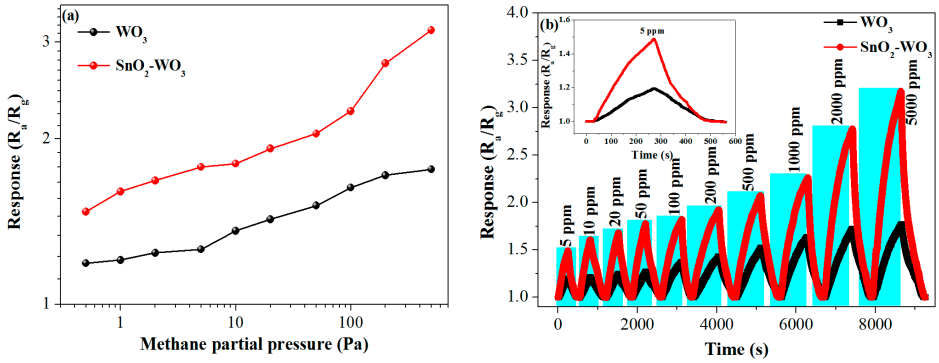

Figure 7. (**a**) Response curve at different methane partial pressures at 90 °C, (**b**) response/recovery curve of pure WO_3 and SnO_2-WO_3 sensors at different methane concentrations at 90 °C.

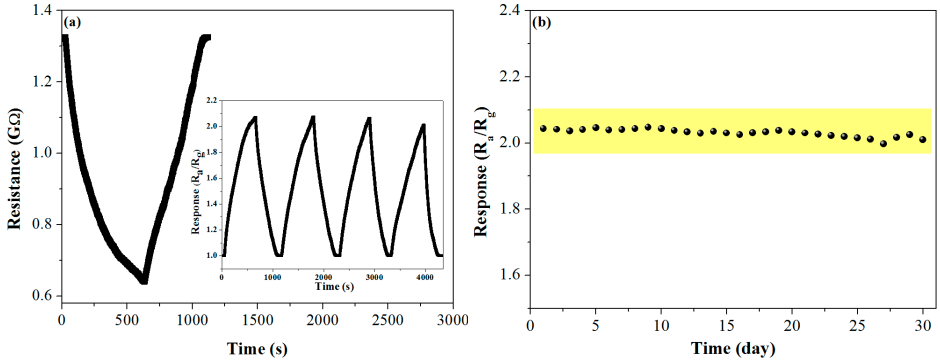

Figure 8. (**a**) Repeatability and (**b**) long-term stability of pure WO_3 and SnO_2-WO_3 sensors towards 500 ppm methane at 90 °C.

3.3. Gas-Sensing Mechanism

The optimum operating temperature for methane detection in this work was relatively low at 90 °C. The stable adsorbed oxygen species on metal oxides was $[O_2^-]$ at low temperatures <200 °C [47]. The basic principle of the gas-sensing mechanism was well described by the receptor function. In air, the atmospheric oxygen was adsorbed on the surface and ionized to be $[O_2^-]$, trapping the electrons from the conduction band of the metal oxides leading to the formation of electron depletion region

at the metal oxide surface. If the metal oxide was a n-type semiconductor, its resistance increased. When the target gas methane was introduced, it reacted with the adsorbed [O_2^-] as follows:

$$CH_4(gas) + 2[O_2^-](adsorbed) \rightarrow CO_2 + 2H_2O + 2e^-$$

releasing the electrons back into the metal oxides. Therefore, the resistance reduced. The response of the metal oxides was based on the resistance change via the oxygen adsorption and desorption.

A specific exposed facet of the sensing material should have specific physical and chemical properties and therefore offer characteristic sensing performance [48–50]. The dominant exposed facet of the WO_3 nanosheets in this work was determined to be the (200) crystal plane as discussed above. Many investigations have been done regarding the comparison among the exposed facets (200), (020) and (002) in WO_3 [51–53]. The (002) crystal plane of γ-WO_3 is an oxygen-terminated facet, which contains exclusively unsaturated coordinated oxygen atoms. The chemisorption of the atmospheric oxygen is beneficial on such a facet, especially with typically rich oxygen vacancies in γ-WO_3 [50,54,55], rising the sensor response. A great number of W atoms are present on the (020) crystal plane, indicating the presence of a great number of dangling bonds, favorable for the sensor performance. The third crystal plane (200) consists of a mixture of O and W atoms and the number of W atoms is less than that on the (020) facet [53]. Possessing both advantages of easy oxygen chemisorption and high reactivity at the dangling bonds of W atoms, the (200) facet shows reasonable sensing response to methane at a relatively low optimum operating temperature of 90 °C.

Both of the WO_3 nanosheets and the SnO_2 nanoparticles were lightly n-doped. Thus, a n–n heterojunction formed at the interface. The band gap E_g was 2.9 eV and 3.7 eV and the electron affinity χ was −3.3 eV and −4.2 eV for WO_3 and SnO_2, respectively [56–58], resulting in $\Delta E_c = -(X_{Sn} - X_W) = 0.9$ eV, $\Delta E_v = -(X_{Sn} + E_{g,Sn} - X_W - E_{g,w}) = 1.7$ eV. The Fermi levels were located slightly above the middle level of the band gap. Band bending occurred at the n–n heterojunction trapping electrons and holes near the interface in SnO_2 and WO_3, respectively, at thermal equilibrium (Figure 9). Subsequently, the higher electron density in the conduction band of SnO_2 at the interface enhanced the local oxygen chemisorption. Otherwise, the lower electron density in WO3 reduced the local chemisorption deteriorating the sensing performance. However, the N_2 adsorption–desorption investigation revealed smaller pore sizes and a larger specific surface area of the SnO_2 nanoparticles as compared to the WO_3 nanosheets as discussed above, which made SnO_2 the dominating phase for oxygen adsorption. Therefore, such a heterojunction improved the performance of the gas sensor. Surely, the much-increased specific surface area by SnO_2 loading enhanced the sensor sensitivity by itself.

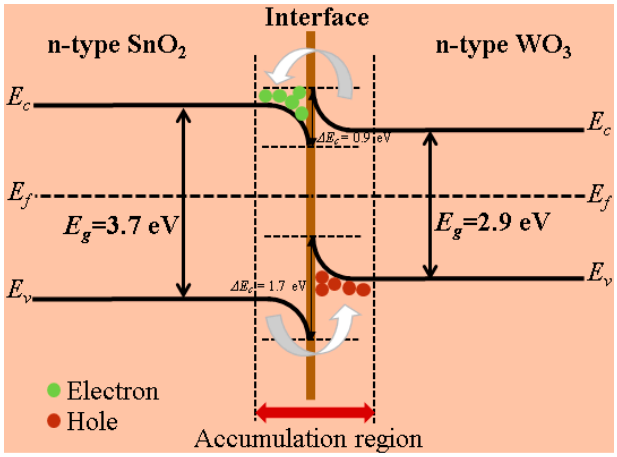

Figure 9. Energy band diagram of the WO_3-SnO_2 (n–n) heterojunction at thermal equilibrium.

The defects formed at the heterojunction could be an additional factor contributing to a better gas-sensing performance. A large lattice mismatch between WO_3 and SnO_2 as observed from the TEM investigation and even the different crystal structures of the monoclinic WO_3 and the rutile SnO_2 resulted in high defect density at the interface. The defects with dangling bonds served as adsorption and highly reactive sites enhancing the sensor sensitivity and a low optimum operating temperature of 90 °C.

4. Conclusions

In summary, SnO_2-loaded WO_3 nanosheets were prepared by a simple impregnation method and a subsequent calcination treatment using SnO_2 and $WO_3.H_2O$ obtained by the hydrothermal method as precursors. The synthesized pure and SnO_2-loaded WO_3 nanosheets had good crystallinity and high purity proved by a series of characterization methods, and SnO_2 nanoparticles with a particle size of about 2 nm were uniformly dispersed on the surface of WO_3 nanosheets. Studies of gas-sensing performance showed that the load of SnO_2 nanoparticles enhanced the sensor sensitivity by a maximum factor of 1.4 as compared to the pure WO_3 nanosheets. Satisfactory repeatability and long-term stability were ensured. The gas-sensing mechanisms were discussed as follows: The observed dominant exposed (200) facet of the WO_3 nanosheets, possessing a good balance between easy oxygen chemisorption and high reactivity at the dangling bonds of W atoms, had a reasonable response value (~1.5) at a low optimum operating temperature (90 °C) without adding any catalyst. Moreover, the electron accumulation layer in SnO_2 enhanced the oxygen adsorption at the surface with SnO_2 as the dominant phase for oxygen adsorption revealed by N_2 adsorption–desorption. The dramatically increased specific surface area from 10.5 m^2/g to 57.7 m^2/g contributed to the improvement of sensor sensitivity as well. Finally, defects formed at the heterojunction were discussed as adsorption and highly reactive sites favorable for gas-sensing performance.

Author Contributions: D.X. conceived and designed the experiments; Y.W., G.S., J.C. and H.B. performed the experiments; J.W. and Z.Z. provided the concept of this research and managed the writing process as the corresponding authors.

Funding: This work was supported by the National Natural Science Foundation of China (U1704255), the Program for Science & Technology Innovation Talents at the Universities of Henan Province (19HASTIT042, 18HASTIT010, 17HASTIT029), the Fundamental Research Funds for the Universities of Henan Province (NSFRF1606, NSFRF1614, NSFRF170201), the Research Foundation for Youth Scholars of Higher Education of Henan Province (2017GGJS053, 2016GGJS-040), the Program for Innovative Research Team of Henan Polytechnic University (T2018-2), and the Foundation for Distinguished Young Scientists of Henan Polytechnic University (J2017-3).

Conflicts of Interest: The authors declare no conflict of interest.

References

1. Cao, J.L.; Qin, C.; Wang, Y.; Zhang, H.L.; Zhang, B.; Gong, Y.X.; Wang, X.D.; Sun, G.; Bala, H.; Zhang, Z.Y. Synthesis of g-C_3N_4 nanosheet modified SnO_2 composites with improved performance for ethanol gas sensing. *RSC Adv.* **2007**, *7*, 25504–25511. [CrossRef]
2. Vuong, N.M.; Hieu, N.M.; Hieu, H.N.; Yi, H.; Kim, D.; Han, Y.-S.; Kim, M. Ni_2O_3-decorated SnO_2 particulate films for methane gas sensors. *Sens. Actuators B Chem.* **2014**, *192*, 327–333. [CrossRef]
3. Amutha, A.; Amirthapandian, S.; Prasad, A.K.; Panigrahi, B.K.; Thangadurai, P. Methane gas sensing at relatively low operating temperature by hydrothermally prepared SnO_2 nanorods. *J. Nanopart. Res.* **2015**, *17*, 1–12. [CrossRef]
4. Nasresfahani, S.; Sheikhi, M.H.; Tohidi, M.; Zarifkar, A. Methane gas sensing properties of Pd-doped SnO_2/reduced graphene oxide synthesized by a facile hydrothermal route. *Mater. Res. Bull.* **2017**, *89*, 161–169. [CrossRef]
5. Chen, W.; Zhou, Q.; Gao, T.; Su, X.; Wan, F. Pd-doped SnO_2-based sensor detecting characteristic fault hydrocarbon gases in transformer oil. *J. Nanomater.* **2013**, *2013*, 1–9. [CrossRef]
6. Kim, K.; Choi, K.; Jeong, H.; Kim, H.J.; Kim, H.P.; Lee, J. Highly sensitive and selective trimethylamine sensors using Ru-doped SnO_2 hollow spheres. *Sens. Actuators B Chem.* **2012**, *166–167*, 733–738. [CrossRef]

7. Wang, D.; Chu, X.; Gong, M. Gas-sensing properties of sensors based on single crystalline SnO_2 nanorods prepared by a simple molten-salt method. *Sens. Actuators B Chem.* **2006**, *117*, 183–187. [CrossRef]
8. Tomer, V.K.; Devi, S.; Malik, R.; Nehra, S.P.; Duhan, S. Fast response with high performance humidity sensing of Ag-SnO_2 /SBA-15 nanohybrid sensors. *Microporous Mesoporous Mater.* **2016**, *219*, 240–248. [CrossRef]
9. Lai, X.; Shen, G.; Xue, P.; Yan, B.; Wang, H.; Li, P.; Xia, W.; Fang, J. Ordered mesoporous NiO with thin pore walls and its enhanced sensing performance for formaldehyde. *Nanoscale* **2015**, *7*, 4005–4012. [CrossRef] [PubMed]
10. Lepoutre, S.; López, B.J.; Sanchez, C.; Amenitsch, H.; Linden, M.; Grosso, D. Nanocasted mesoporous nanocrystalline ZnO thin films. *J. Mater. Chem.* **2010**, *20*, 537–542. [CrossRef]
11. Duhan, S.; Tomer, V.K. Mesoporous silica: Making "sense" of sensors. In *Advanced Sensor and Detection Materials*; Tiwari, A., Demir, M.M., Eds.; Scrivener Publishing: Linkoping, Sweden, 2014; pp. 149–192.
12. Zhao, J.; Wang, W.; Liu, Y.; Ma, J.; Li, X.; Du, Y.; Lu, G. Ordered mesoporous Pd/SnO_2 synthesized by a nanocasting route for high hydrogen sensing performance. *Sens. Actuators B* **2011**, *160*, 604–608. [CrossRef]
13. Chen, Y.; Yu, L.; Feng, D.; Zhuo, M.; Zhang, M.; Zhang, E.; Xu, Z.; Li, Q.; Wang, T. Superior ethanol-sensing properties based on Ni-doped SnO_2 p-heterojunction hollow spheres. *Sens. Actuators B* **2012**, *166*, 61–67. [CrossRef]
14. Akiyama, M.; Tamaki, J.; Miura, N.; Yamazoe, N. Tungsten oxide-based semiconductor sensor highly sensitive to NO and NO_2. *Chem. Lett.* **1991**, *1991*, 1611–1614. [CrossRef]
15. Rothschild, A.; Komem, Y. The effect of grain size on the sensitivity of nanocrystalline metal-oxide gas sensors. *J. Appl. Phys.* **2004**, *95*, 6374–6380. [CrossRef]
16. Korotcenkov, G. The role of morphology and crystallographic structure of metal oxides in response of conductometric-type gas sensors. *Mater. Sci. Eng. R* **2008**, *61*, 1–39. [CrossRef]
17. Tamaki, J.; Hashishin, T.; Uno, Y.; Dao, D.V.; Sugiyama, S. Ultrahigh-sensitive WO_3 nanosensor with interdigitated Au nanoelectrode for NO_2 detection. *Sens. Actuators B* **2008**, *132*, 234–238. [CrossRef]
18. Choi, Y.G.; Sakai, G.; Shimanoe, K.; Yamazoe, N. Wet process- based fabrication of WO_3 thin film for NO_2 detection. *Sens. Actuators B* **2004**, *101*, 107–111. [CrossRef]
19. Zhou, L.; Zou, J.; Yu, M.; Lu, P.; Wei, J.; Qian, Y.; Wang, Y.; Yu, C. Green synthesis of hexagonal-shaped WO_3 0.33 H_2O nanodiscs composed of nanosheets. *Cryst. Growth Des.* **2008**, *8*, 3993–3998. [CrossRef]
20. Liu, Z.; Miyauchi, M.; Yamazaki, T.; Shen, Y. Facile synthesis and NO_2 gas sensing of tungsten oxide nanorods assembled microspheres. *Sens. Actuators B* **2009**, *140*, 514–519. [CrossRef]
21. Cao, B.; Chen, J.; Tang, X.; Zhou, W. Growth of monoclinic WO_3 nanowire array for highly sensitive NO_2 detection. *J. Mater. Chem.* **2009**, *19*, 2323–2327. [CrossRef]
22. Zhu, L.F.; She, J.C.; Luo, J.Y.; Deng, S.Z.; Chen, J.; Xu, N.S. Study of physical and chemical processes of H_2 sensing of Pt-coated WO_3 nanowire films. *J. Phys. Chem. C* **2010**, *114*, 15504–15509. [CrossRef]
23. Cho, Y.H.; Kang, Y.C.; Lee, J.H. Highly selective and sensitive detection of trimethylamine using WO_3 hollow spheres prepared by ultrasonic spray pyrolysis. *Sens. Actuators B* **2013**, *176*, 971–977. [CrossRef]
24. Li, X.L.; Lou, T.J.; Sun, X.M.; Li, Y.D. Highly sensitive WO_3 hollow-sphere gas sensors. *Inorg. Chem.* **2004**, *43*, 5442–5449. [CrossRef] [PubMed]
25. Wang, W.S.; Zhen, L.; Shao, W.Z.; Chen, Z.L. Sodium chloride induced formation of square-shaped cadmium molybdate nanoplates. *Mater. Lett.* **2014**, *131*, 292–294. [CrossRef]
26. Zhang, J.Y.; Ding, E.J.; Xu, S.C.; Li, Z.H.; Wang, X.X.; Song, F. Sensitization of an optical fiber methane sensor with graphene. *Opt. Fiber Technol.* **2017**, *37*, 26–29. [CrossRef]
27. Alaya, M.N.; Rabah, M.A. Surface acidity and catalytic activity of aged SO_4^{2-} /SnO_2 catalyst supported with WO_3. *J. Alloys Compd.* **2013**, *575*, 285–291. [CrossRef]
28. Liu, L.; Song, P.; Wei, Q.; Zhong, X.; Yang, Z.; Wang, Q. Synthesis of porous SnO_2 hexagon nanosheets loaded with Au nanoparticles for high performance gas sensors. *Mater. Lett.* **2017**, *201*, 211–215. [CrossRef]
29. Guo, J.; Zhang, J.; Gong, H.; Ju, D.; Cao, B. Au nanoparticle-functionalized 3D SnO_2 microstructures for high performance gas sensor. *Sens. Actuators B Chem.* **2016**, *226*, 266–272. [CrossRef]
30. Kolhe, P.S.; Koinkar, P.M.; Maiti, N.; Sonawane, K.M. Synthesis of Ag doped SnO_2 thin films for the evaluation of H_2S gas sensing properties. *Phys. B Condens. Matter* **2017**, *524*, 90–96. [CrossRef]
31. Liu, Y.; Huang, J.; Yang, J.; Wang, S. Pt nanoparticles functionalized 3D SnO_2 nanoflowers for gas sensor application. *Solid. State. Electron.* **2017**, *130*, 20–27. [CrossRef]

32. Li, Y.; Deng, D.; Chen, N.; Xing, X.; Liu, X.; Xiao, X.; Wang, Y. Pd nanoparticles composited SnO_2 microspheres as sensing materials for gas sensors with enhanced hydrogen response performances. *J. Alloys Compd.* **2017**, *710*, 216–224. [CrossRef]
33. Urasinska-Wojcik, B.; Vincent, T.A.; Chowdhury, M.F.; Gardner, J.W. Ultrasensitive WO_3 gas sensors for NO_2 detection in air and low oxygen environment. *Sens. Actuators B Chem.* **2017**, *239*, 1051–1059. [CrossRef]
34. Shendage, S.S.; Patil, V.L.; Vanalakar, S.A.; Patil, S.P.; Harale, N.S.; Bhosale, J.L.; Kim, J.H.; Patil, P.S. Sensitive and selective NO_2 gas sensor based on WO_3 nanoplates. *Sens. Actuators B Chem.* **2017**, *240*, 426–433. [CrossRef]
35. Miller, D.R.; Akbar, S.A.; Morris, P.A. Nanoscale metal oxide-based heterojunctions for gas sensing: A review. *Sens. Actuators B* **2017**, *204*, 250–272. [CrossRef]
36. Gong, Y.; Wang, Y.; Sun, G.; Jia, T.K.; Jia, L.; Zhang, F.M.; Lin, L.; Zhang, B.; Cao, J.L.; Zhang, Z. Carbon nitride decorated ball-flower like Co_3O_4 hybrid composite: Hydrothermal synthesis and ethanol gas sensing application. *Nanomaterials* **2018**, *8*, 132. [CrossRef] [PubMed]
37. Cao, J.L.; Gong, Y.X.; Wang, Y.; Zhang, B.; Zhang, H.L.; Sun, G.; Bala, H.; Zhang, Z.Y. Cocoon-like ZnO decorated graphitic carbon nitride nanocomposite: Hydrothermal synthesis and ethanol gas sensing application. *Mater. Lett.* **2017**, *198*, 76–80. [CrossRef]
38. Xue, D.P.; Wang, Y.; Cao, J.L.; Zhang, Z.Y. Hydrothermal synthesis of CeO_2-SnO_2 nano-flowers for improving triethylamine gas sensing property. *Nanomaterials* **2018**, *8*, 1025. [CrossRef] [PubMed]
39. Sun, G.; Chen, H.; Li, Y.; Chen, Z.; Zhang, S.; Ma, G.; Jia, T.; Cao, J.; Bala, H.; Wang, X.; et al. Synthesis and improved gas sensing properties of NiO-decorated SnO_2 microflowers assembled with porous nanorods. *Sens. Actuators B Chem.* **2016**, *233*, 180–192. [CrossRef]
40. Wang, Y.J.; Wang, Q.S.; Zhan, X.Y.; Wang, F.M.; Safdar, M.; He, J. Visible light driven type II heterostructures and their enhanced photocatalysis properties: A review. *Nanoscale* **2013**, *5*, 8326–8339. [CrossRef] [PubMed]
41. Xiao, Y.; Yang, Q.; Wang, Z.; Zhang, R.; Gao, Y.; Sun, P.; Sun, Y.; Lu, G. Improvement of NO_2 gas sensing performance based on discoid tin oxide modified by reduced graphene oxide. *Sens. Actuators B* **2016**, *227*, 419–426. [CrossRef]
42. Mizsei, J. Semiconducting gas sensor incorporating a sparking decomposer. *Sens. Actuators B* **1990**, *2*, 199–203. [CrossRef]
43. Mizsei, J. How can sensitive and selective semiconductor gas sensors be made? *Sens. Actuators B* **1995**, *23*, 173–176. [CrossRef]
44. Navazani, S.; Shokuhfar, A.; Hassanisadi, M.; Askarieh, M.; Carlo, A.D.; Agresti, A. Facile synthesis of a SnO_2@rGO nanohybrid and optimization of its methane-sensing parameters. *Talanta* **2018**, *181*, 422–430. [CrossRef] [PubMed]
45. Galstyan, V.; Comini, E.; Kholmanov, I.; Faglia, G.; Sberveglieri, G. Reduced graphene oxide/ZnO nanocomposite for application in chemical gas sensors. *RSC Adv.* **2016**, *6*, 34225–34232. [CrossRef]
46. Ahmad, Z.U.; Yao, L.; Wang, J.; Gang, D.D.; Islam, F.; Lian, Q.; Zappi, M.E. Neodymium embedded ordered mesoporous carbon (OMC) for enhanced adsorption of sunset yellow: Characterizations, adsorption study and adsorption mechanism. *Chem. Eng. J.* **2019**, *359*, 814–826. [CrossRef]
47. Yamazoe, N.; Shimanoe, K. Theory of power laws for semiconductor gas sensors. *Sens. Actuators B* **2008**, *128*, 566–573. [CrossRef]
48. Kida, T.; Nishiyama, A.; Hua, Z.; Suematsu, K.; Yuasa, M.; Shimanoe, K. WO_3 nanolamella gas sensor: Porosity control using SnO_2 nanoparticles for enhanced NO_2 sensing. *Langmuir* **2014**, *30*, 2571–2579. [CrossRef] [PubMed]
49. Cao, S.; Chen, H. Nanorods assembled hierarchical urchin-like WO_3 nanostructures: Hydrothermal synthesis, characterization, and their gas sensing properties. *J. Alloys Compd.* **2017**, *702*, 644–648. [CrossRef]
50. Yin, M.; Yao, Y.; Fan, H.; Liu, S. WO_3-SnO_2 nanosheet composites: Hydrothermal synthesis and gas sensing mechanism. *J. Alloys Compd.* **2018**, *736*, 322–331. [CrossRef]
51. Jia, Q.-Q.; Ji, H.-M.; Wang, D.-H.; Bai, X.; Sun, X.-H.; Jin, Z.-G. Exposed facets induced enhanced acetone selective sensing property of nanostructured tungsten oxide. *J. Mater. Chem. A* **2014**, *2*, 13602–13611. [CrossRef]
52. Zhu, J.; Wang, S.; Xie, S.; Li, H. Hexagonal single crystal growth of WO_3 nanorods along a [110] axis with enhanced adsorption capacity. *Chem. Commun.* **2011**, *47*, 4403–4405. [CrossRef] [PubMed]

53. Han, X.; Han, X.; Li, L.; Wang, C. Controlling the morphologies of WO_3 particles and tuning the gas sensing properties. *New J. Chem.* **2012**, *36*, 2205–2208. [CrossRef]
54. Xiao, B.; Wang, D.; Wang, F.; Zhao, Q.; Zhai, C.; Zhang, M. Preparation of hierarchical WO_3 dendrites and their applications in NO_2 sensing. *J. Alloys Compd.* **2017**, *43*, 8183–8189.
55. Li, H.; Liu, B.; Cai, D.P.; Wang, Y.; Liu, Y.; Mei, L.; Wang, L.; Wang, D.; Li, Q.; Wang, T. High-temperature humidity sensors based on WO_3-SnO_2 composite hollow nanospheres. *J. Mater. Chem. A* **2014**, *2*, 6854–6862. [CrossRef]
56. Wang, F.; di Valentin, C.; Pacchioni, G. Electronic and structural properties of WO_3: A systematic hybrid DFT study. *J. Phys. Chem. C* **2011**, *115*, 8345–8353. [CrossRef]
57. Floriano, E.A.; Scalvi, L.V.A.; Saeki, M.J.; Sambrano, J.R. Preparation of TiO_2/SnO_2 thin films by sol-gel method and periodic B3LYP simulations. *J. Phys. Chem. A* **2014**, *118*, 5857–5865. [CrossRef] [PubMed]
58. Sukunta, J.K.; Wisitsoraat, A.; Tuantranont, A.; Phanichphant, S.K.; Liewhiran, C.K. WO_3 nanotubes-SnO_2 nanoparticles heterointerfaces for ultrasensitive and selective NO_2 detections. *Appl. Surf. Sci.* **2018**, *458*, 319–332. [CrossRef]